Thin–Walled Structures 222 (2026) 114563

Contents lists available at ScienceDirect

Thin-Walled Structures

journal homepage: www.elsevier.com/locate/tws

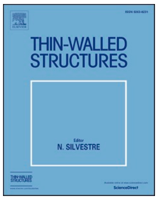

Full length article

Viscoelastic damping design - Experimental analysis of optimized constrained layer damping treatments at different ambient temperatures

Martin Gröhlich [a,b,*], Marc Böswald [a,b], Jörg Wallaschek [c]

[a] German Aerospace Center (DLR), Institute of Aeroelasticity, Bunsenstraße 10, 37073, Göttingen, Germany
[b] Cluster of Excellence SE^{2}A - Sustainable and Energy-Efficient Aviation, Technical University Braunschweig, Germany
[c] Leibniz University Hannover, Institute of Dynamics and Vibration Research (IDS) An der Universität 1, 30823, Garbsen, Germany

ARTICLE INFO

Keywords:
Constrained layer damping
Viscoelastic damping
Experimental modal analysis
Optimized damping design

ABSTRACT

Constrained Layer Damping (CLD) is an established technology for passive vibration damping. Vibrational energy is dissipated by forcing a viscoelastic material into shear strain. However, the damping performance of CLD treatments is highly dependent on the temperature and the design of such structures can be tailored to operational conditions.

This paper presents an experimental analysis of shape-optimized CLD treatments over a temperature range from -20 °C to +20 °C. The samples were designed and manufactured with respect to maximum damping of the first bending mode at minimum and maximum temperature. Eigenfrequencies and damping ratios identified from a modal test in a climatic chamber are compared with those obtained from numerical simulations. The comparison shows a good correlation of the modal parameters. The results demonstrate that using the widths of virtually segmented core and face layers as design parameters is a valid approach for shape optimization of CLD treatments. Furthermore, it is proven that the optimal shape of a CLD treatment is temperature-dependent and that its damping performance varies with the ambient temperature condition.

1. Introduction

Due to their lightweight design, thin-walled structures are prone to vibration. A prominent example of sophisticated lightweight design is an aircraft fuselage. A fuselage is composed of individual components, such as the thin skin field and beam-like frames or stringers with thin-walled profiles [1]. Under operational conditions, structural vibrations lead to sound radiation which is perceived as disturbing noise by the passengers. Therefore, in order to improve the cabin comfort, attenuation technologies counteracting vibration problems have been developed and applied in the past decades. The spectrum of countermeasures for thin-walled structures reaches from vibration absorbers [2–4], active structural-acoustic control systems [5] and vibration isolators [6,7] to the application of meta-structures [8,9].

Another opportunity is to dissipate vibrational energy by means of materials with inherent viscoelastic properties, such as elastomers. The behavior of these materials is typically frequency- and temperature-dependent. Their properties are characterized in a dynamic mechanical analysis (DMA) and appropriate mathematical models are fitted to the data afterwards [10]. Prominent material models for approximating the frequency dependence are the generalized Maxwell model (GMM) known as Prony series [11], the model of fractional derivatives [12] and the Golla-Hughes-McTavish model [13]. In contrast, the temperature dependence is considered by the Williams-Landel-Ferry (WLF) equation [14]. The material models allow for the mathematical analysis in the design process of attenuation technologies.

In this context, Constrained Layer Damping (CLD) has been proven to be an effective damping treatment [15,16]. Fig. 1 demonstrates the basic principle of a CLD treatment. A viscoelastic layer exhibiting high damping properties is constrained between a host structure and a stiff face layer. In the case of bending vibrations, the core layer is forced into shear deformation and dissipates vibrational energy. This technology encompasses passive, active and hybrid treatments. In active or hybrid systems, the shear mechanism is supported by piezoelectric actuators [17]. While active treatments need to be supplied by an energy source, concomitant with additional mass, passive treatments work autonomously under operational condition. This paper focusses on passive CLD treatments.

The fundamental theory of CLD treatments has been studied by many scholars [18–21]. Later on, with the establishment of the Finite Element

---

* Corresponding author.
E-mail address: Martin.Groehlich@dlr.de (M. Gröhlich).

https://doi.org/10.1016/j.tws.2026.114563
Received 10 April 2025; Received in revised form 21 November 2025; Accepted 19 January 2026

Method (FEM) as an engineering tool, research activities focused on the maximization of damping. Topology optimization became a popular method that has been applied in a multitude of studies [22–26]. In addition, alternative approaches have been published for enhancing damping of CLD treatments. For instance, Lepoittevin and Kress [27] determined the amount and optimal positions of cuts in the core and face layer. Araujo et al. [28] optimized the ply angle and thicknesses of laminated layers, while Xu et al. [29] optimized the size, thickness and position of a damping patch placed on a cylindrical structure.

Recently, we have proposed another approach for shape optimization of CLD beams [30]. Virtually dividing the structure into several segments and using the width of each segment as a design parameter, leads to an efficient damping design. Different temperatures and a characterized bromobutyl rubber were considered in the analyses. As a result, the optimal design as well as the damping performance turned out to be temperature-dependent. However, the previous work lacked in experimental evidence of the numerical results. The following paper addresses these gaps and provides a comparison between numerical and experimental results obtained by a modal test in a climatic chamber.

In this regard, the literature encompasses extensive works, considering the comparison between analytically or numerically and experimentally determined modal parameters of CLD treatments [25,31–35], also including the analysis of temperature-related effects [36,37]. Larger deviations were reported mostly for the damping ratio (or loss factor) with more than 30 % (relative value) [31], whereas the accuracy of the eigenfrequency is better. According to [36], this effect can be traced back to a higher sensitivity of the damping ratio to environmental and numerical influences.

The content of the paper is structured as follows: Section 1 provided a short introduction. The fundamentals of viscoelastic damping and methods for the analysis of viscoelastic systems are presented in Section 2. Section 3 presents the shape-optimized CLD samples and the basic setup of the experimental and numerical analyses. Finally, the results of the analyses are presented and discussed in Section 4. The paper ends with a conclusion in Section 5. Preliminary data was published in a PhD thesis [38] in German language and is now enhanced and rephrased in English.

2. Theoretical background of viscoelastic damping

This section provides a brief overview of the fundamentals of viscoelastic damping. The first subsection deals with the mathematical modeling of frequency- and temperature-dependent viscoelastic behavior, while the second subsection explains methods to determine the eigenfrequencies and damping ratios in numerical and experimental analyses. Part of the theory presented in this section has been published previously in [30]. Nevertheless, the theory is summarized for a better comprehension. More general and more detailed overviews of this topic can be found in [11,39].

2.1. Modeling of viscoelastic materials

Viscoelastic materials exhibit frequency- and temperature-dependent behavior. Considering harmonic steady-state excitation, the linear viscoelastic properties are expressed in terms of a complex modulus E^*

$$E^*(\omega,T) = E'(\omega,T) + \mathrm{i}E''(\omega,\mathrm{T}), \tag{1}$$

where ω is the angular frequency, T is the temperature and i is the imaginary unit. The storage modulus E' indicates the elastic property, while the loss modulus E'' represents the viscous property. The key parameter for assessing the damping capability of a linear viscoelastic material is the ratio of the loss and storage moduli, referred to as the material loss factor $\tan(\delta)$

$$\tan(\delta(\omega,T)) = \frac{E''(\omega,T)}{E'(\omega,T)}. \tag{2}$$

The GMM is an appropriate mechanical substitution model for approximating the frequency dependence of the complex modulus. In this case, the storage and loss moduli are defined as a Prony series consisting of several relaxation times τ_i and elastic moduli E_i obtained from curve fitting of measured DMA data

$$E'(\omega) = E_\infty + \sum_{i=1}^{n} E_i \frac{\omega^2\tau_i^2}{1+\omega^2\tau_i^2}, \tag{3}$$

$$E''(\omega) = \sum_{i=1}^{n} E_i \frac{\omega\tau_i}{1+\omega^2\tau_i^2}. \tag{4}$$

In Eq. (3), the long-term modulus E_∞ corresponds to the elastic behavior under quasi-static deformation ($\omega \to 0$). It is emphasized that a complex shear modulus G^* is often used in the literature to describe the material properties. Assuming isotropy and using Poisson's ratio ν, the following relationship applies

$$E^* = 2G^*(1+\nu). \tag{5}$$

Due to the chemical composition of elastomers, the mechanical behavior at low frequencies is similar to that at high temperatures and vice versa. This phenomenon, known as time-temperature superposition, enables shifting the frequency-dependent material curves and thus, determining the material properties at specific temperatures. For rheologically simple materials, a shift along the frequency axis can be performed by a horizontal shift factor a_T, resulting from the WLF equation [14,40]

$$\log_{10}(a_T) = \log_{10}\left(\frac{f_{\mathrm{ref}}}{f}\right) = \frac{-C_1 \cdot \Delta T}{C_2 + \Delta T}, \tag{6}$$

where the parameters C_1 and C_2 are fitting parameters and ΔT is the difference between the temperature of interest and the reference temperatures ($\Delta T = T - T_{\mathrm{ref}}$). For instance, the loss modulus at a temperature T and at a frequency f is the same as the loss modulus at a reference temperature T_{ref} and at a reference frequency $f_{ref} = \alpha_T \cdot f$. If the elastomer is filled with carbon black, the Payne effect [41,42] occurs, which is included in the time-temperature analogy by an additional vertical shift. The vertical shift is considered as an Arrhenius-like activation

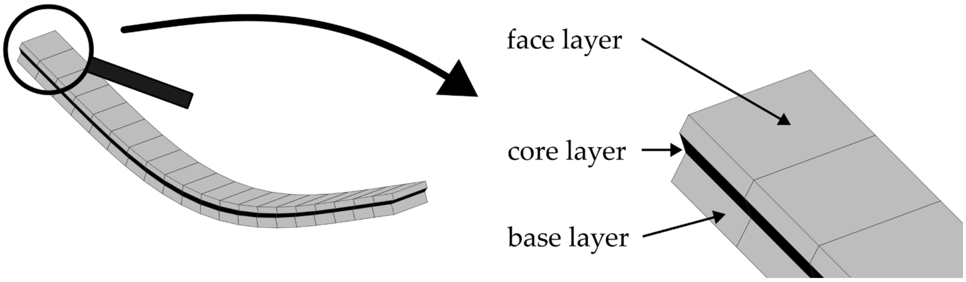

Fig. 1. First bending mode of a CLD beam and shear deformation of the viscoelastic core layer.

process and the corresponding shift factor b_T can be calculated from the apparent activation energy E_A and the universal gas constant R [43]

$$b_T \approx \exp\left(\frac{E_A}{R}\left(\frac{1}{T}-\frac{1}{T_{\mathrm{ref}}}\right)\right). \tag{7}$$

By incorporating the vertical and horizontal shift factors, the material properties can be determined for specific temperatures and frequencies

$$\begin{aligned} E^{'}(f,T) &\rightarrow b_{T,E^{'}} \cdot E^{'}\left(f_{\mathrm{ref}}, T_{\mathrm{ref}}\right) \\ E^{''}(f,T) &\rightarrow b_{T,E^{''}} \cdot E^{''}\left(f_{\mathrm{ref}}, T_{\mathrm{ref}}\right). \end{aligned} \tag{8}$$

It should be noted that the activation energies for storage and loss modulus may be different. The interested reader is referred to [40] for more detailed information on the chemical background and the application of the shift process.

2.2. Numerical and experimental determination of modal parameters

The identification of modal parameters such as eigenfrequencies and damping ratios of viscoelastically damped systems is of great importance for the validation of structural systems. Two approaches used in this paper are described below: One for numerical analyses and one for experimental analyses.

Numerical approach

The eigenvalue problem of a system with frequency-dependent viscoelastic properties is of the form [44]

$$\left[\mathbf{K}^*\left(\lambda_r^*\right) - \lambda_r^{*^2}\mathbf{M}\right]\boldsymbol{\phi}_r^* = \mathbf{0}, \tag{9}$$

where $\mathbf{M}$ denotes the mass matrix, $\mathbf{K}^*$ the complex and frequency-dependent stiffness matrix, λ_r^* the complex eigenvalue of mode r and $\boldsymbol{\phi}_r^*$ the corresponding complex eigenvector. The complex nature of the stiffness matrix is due to the complex viscoelastic properties, being propagated through the FE formulation. More information on the composition of the complex stiffness matrix can be found in [40]. According to [44], the eigenvalue of a viscoelastically damped system is calculated by

$$\lambda_r^{*^2} = \omega_r^2(1+\mathrm{i}\eta_r). \tag{10}$$

The real part contains information about the eigenfrequency ω_r, while the damping is related to the modal loss factor η_r. The modal loss

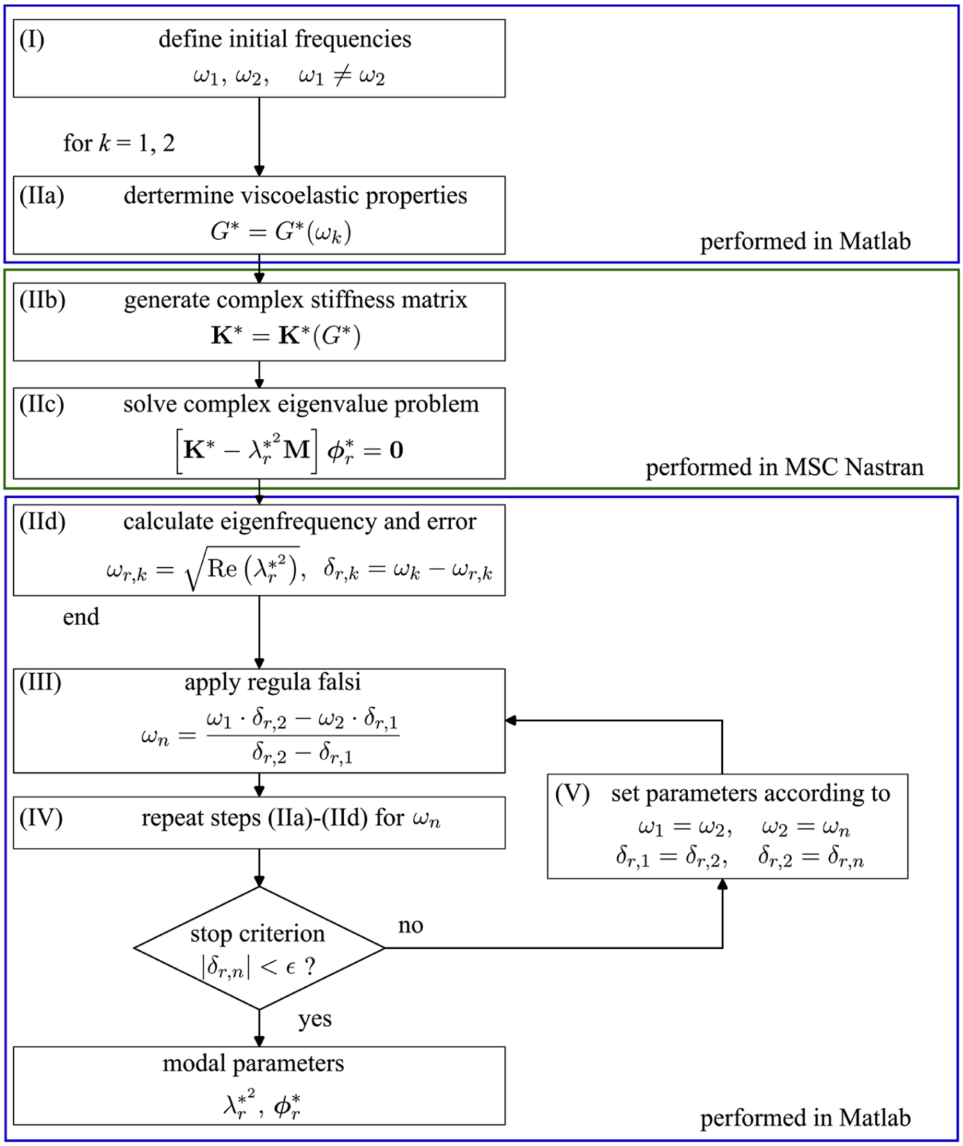

Fig. 2. Flowchart of the iterative eigenvalue solver, taken from [30].

factor is the ratio of the imaginary and real part of the eigenvalue

$$\eta_r = \frac{\mathrm{Im}\left(\lambda_r^{*^2}\right)}{\mathrm{Re}\left(\lambda_r^{*^2}\right)}. \tag{11}$$

It is important to emphasize the difference between the modal loss factor and the material loss factor. Whereas the modal loss factor η_r quantifies the damping of a mode as a system property, the material loss factor $\tan(\delta)$ quantifies the material damping as a material property. It should also be noted that for weakly damped systems, the modal loss factor can be converted to the damping ratio D_r by [45]

$$2D_r \approx \eta_r. \tag{12}$$

This relationship will be used later to compare the numerical and experimental results.

Solving the eigenvalue problem of Eq. (9) is not straightforward due to the frequency-dependent stiffness matrix. However, some suitable analysis methods are available and reviewed by Vasques et al. [39] and compared by Rouleau et al. [44]. In this paper, an iterative eigenvalue solver (IES) is applied, whose constitutive algorithm is based on the regula falsi method. The IES has been used in previous studies [30,40]. Fig. 2 shows a flowchart of the IES.

First, two initial frequencies are defined (I). For each of these frequencies, the viscoelastic material properties are determined (IIa), the complex stiffness matrix is generated (IIb) and the complex eigenvalue problem is solved (IIc). Afterwards, the corresponding eigenfrequencies are computed and the absolute error δ_r between the initial frequency and the eigenfrequency is calculated (IId). The results are transferred to the regula falsi method, where an optimized frequency is estimated (III). In step (IV), the previous steps (IIa) - (IId) are repeated for the optimized frequency. If the stop criterion (threshold ε) does not apply, the parameters are changed as described for step (V). Otherwise, the eigenvalue and eigenvector are found and the modal parameters can be calculated by Eq. (10).

Experimental approach

The experimental approach to obtain the modal parameters is to analyze the frequency response functions (FRFs) using appropriate modal identification methods. This approach is known as experimental modal analysis. The bandwidth of identification methods reaches from time domain to frequency domain-based approaches, which are subdivided into single- and multiple degrees of freedom methods. An overview of existing identification methods can be found in [46,47]. In this paper, the Least-Squares Complex Frequency domain (LSCF) method is used in the context of the PolyMAX algorithm [48,49].

The method performs experimental modal analysis in three steps, where the first step is the most relevant in the context of this paper. In this step, the eigenvalues s_r are identified from the FRFs. A mathematical representation of the FRF H_{kl} as rational-fraction polynomials is used in the Laplace domain

$$H_{kl}(s) = \frac{\sum_{r=0}^{n} b_{kl,r} s^r}{\sum_{r=0}^{n} d_r s^r} \tag{13}$$

and fitted to the measured FRFs. The subscript kl refers to the response degree of freedom k and to the excitation degree of freedom l. The polynomial coefficients b_r and d_r are identified at first, where the coefficients of the denominator polynomial are of particular interest. Afterwards, the eigenvalues can be obtained from the roots of the denominator polynomial. The poles comprise the information about eigenfrequency and damping ratio

$$s_r = -\omega_r D_r \pm \mathrm{i}\omega_r\sqrt{1 - D_r^2}. \tag{14}$$

The two remaining steps encompass the calculation of the residuals based on the determined eigenvalues as well as the identification of the mode shape vectors and the modal scaling constant. Since these parameters are not relevant for this paper, the interested reader is referred to [47] for information about the theory.

3. Experimental and numerical analyses

This section introduces the shape-optimized CLD specimens and describes the procedure of the experimental and numerical analyses. The objective of the analyses is a comparison of the experimental and numerical eigenfrequencies and damping ratios at different temperatures.

3.1. Shape-optimized CLD specimens

Two shape-optimized CLD samples, shown in Fig. 3, were manufactured based on the results of the numerical optimization performed in [30]. Both samples were designed for maximum damping of the first bending mode, the upper sample for -20 °C and the lower sample for +20 °C. In the following, these specimens will be indicated as Opt253 and Opt293, respectively. The shapes consist of eight sections with different widths (the width of the outmost segment is zero for both samples) which are designed symmetric to the painted dashed lines. Each segment has a length of 25 mm and a width given in the figure. It can be seen that the shapes are almost oppositional. While most of the CLD material is added around the center region for Opt253, the major part of the CLD material is added at the outer regions for Opt293.

The base and the face layer consist of aluminum ($E'_{\mathrm{Alu}} = 70$ GPa, $\nu_{\mathrm{Alu}} = 0.33$, $\tan\delta_{\mathrm{Alu}} = 0.005$ and $\rho_{\mathrm{Alu}} = 2660\ \mathrm{kg/m^3}$, where ρ is the density) with mean thicknesses corresponding to $t_{\mathrm{base}} = 8.06$ mm and $t_{\mathrm{face}} = 5.07$ mm. The core layers of the CLD treatments were fabricated from a bromobutyl elastomer (BIIR) and were conglutinated by Loctite 480 to the adjacent layers. Loctite 480 was selected because it is compatible with the elastomer and stiff enough to transmit the shear forces between the adjacent layers. The elastomer was designed, vulcanized and characterized by the Deutsches Institut für Kautschuktechnologie. The thicknesses of the core layers deviate from the numerical layout due to creeping effects during the vulcanization and correspond to $t_{\mathrm{core}} = 1.87$ mm for Opt253 and $t_{\mathrm{core}} = 1.79$ mm for Opt293, respectively.

The material was characterized based on DMA data. Fig. 4 shows the application of the time-temperature superposition of DMA data measured at different temperatures. It can be seen that a continuous master curve for 20 °C (a) is generated by shifting the individual DMA data points (b) along the frequency axis and, less pronounced, along the modulus axis. Not all measured temperatures are displayed in the diagram for the purpose of clarity. Subsequently, a Prony series was fitted to the master curve. Fig. 5 shows a comparison of the experimental and synthesized master curves of BIIR for a reference temperature of 20 °C. It can be seen that the master curve of the storage modulus is adequately approximated. In contrast, the synthetic curve of the loss factor shows larger deviations behind the peak above a frequency of 10 kHz. This effect can be traced back to the small number of DMA data points at low temperatures and high frequencies, respectively. As a result, the curve fit of lower frequencies is weighted more strongly at the expense of inaccuracies in the higher frequency domain. As a consequence, the loss factor of the material above this frequency is underestimated by the Prony series. The model parameters of the Prony series and WLF- and Arrhenius equations are listed in Tables A and B in the appendix. A detailed description of the DMA and the characterization is given in [40]. Furthermore, the density of BIIR corresponds to a value of $\rho_{\mathrm{BIIR}} = 1114\ \mathrm{kg/m^3}$, while the Poisson's ratio is $\nu_{\mathrm{BIIR}} = 0.499$.

3.2. Experimental analysis

The experimental analysis was performed as a modal impact test in a

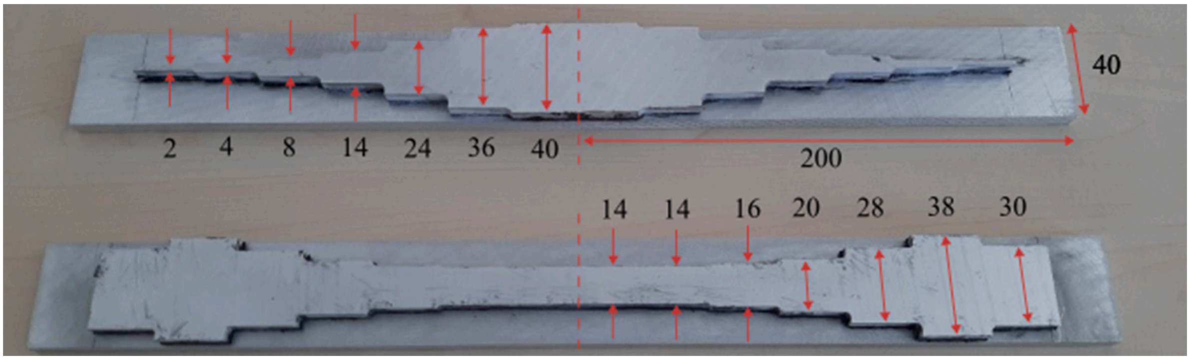

Fig. 3. Samples Opt253 (top) and Opt293 (bottom). The dashed lines indicate the symmetry lines, numbers are displayed in mm.

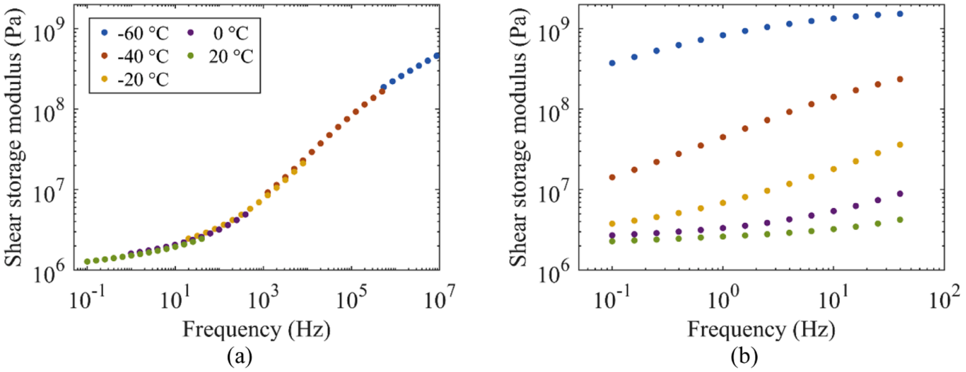

Fig. 4. Composition of the master curve at 20 °C (a) by applying the time-temperature superposition to DMA data points measured at different temperatures (b).

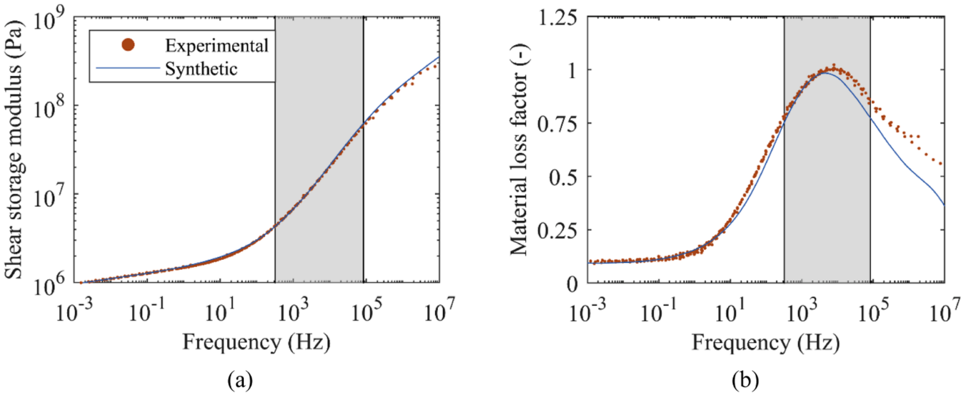

Fig. 5. Comparison of experimental and synthetic master curves of (a) shear storage modulus and (b) material loss factor of BIIR at a reference temperature of 20 °C. The shaded areas indicate the relevant frequency range with respect to the identified eigenfrequencies from the modal test in Section 4.

climatic chamber with a setup illustrated in Fig. 6. All specimens were suspended from a rigid frame. Three acceleration sensors (PCB 352C22) are mounted at the lower corners of each structure. In this case, the small number of sensors is sufficient to distinguish between bending and torsional modes by evaluating the imaginary part of each FRF. The samples were excited by an automatic modal hammer (Maul-Theet vImpact-61) from the backside. In addition, a temperature sensor was mounted at the frame to monitor the current temperature. Five temperatures (-20 °C, -10 °C, 0 °C, 10 °C and 20 °C) were chosen and subsequently adjusted in the climatic chamber. The temperature control and the opening of the climatic chamber for readjusting the sensors and the modal hammer caused deviations between the target and actually measured temperature. Therefore, an average value has been calculated for the temperature. Table 1 lists the target and the computed mean temperatures. The temperature was sampled every 10 s during the measurement.

Time data was acquired using the Siemens Simcenter SCADAS Mobile data acquisition system with a 24-bit A/D converter which was placed outside the chamber. The measurement time was set to 2 s per impact and the time signals were sampled with a sampling frequency of 8192 Hz. Since the lowest mode was expected to appear highly damped above 200 Hz, a full decay of the vibrations was estimated in 2 s. Therefore, it was not necessary to apply exponential windowing to the response signal. Instead, a rectangular window was applied to the force signal. Signal processing was performed automatically by the Siemens Simcenter Testlab software. Afterwards, the PolyMAX algorithm was used to identify the eigenfrequencies and modal damping ratios from the computed and averaged FRFs. The PolyMAX algorithm is based on the

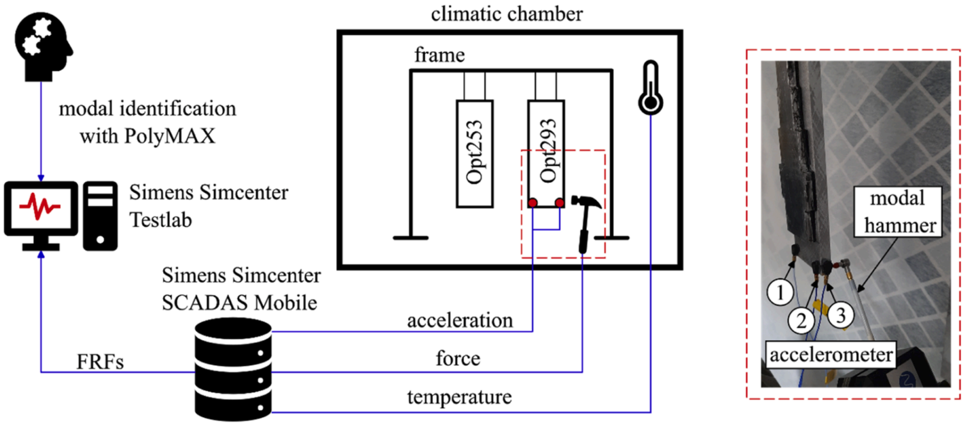

Fig. 6. Experimental setup of the impact test.

Table 1
Target and measured mean temperatures.

Target temperature (°C)	-20	-10	0	10	20
Measured temperature (°C)	-19.8	-10.5	0.5	9.2	18.7

LSCF method referred to in Section 2.2.

Fig. 7 (a) and (b) show FRFs of Opt253 and Opt293 for all measured temperatures. It can be seen that the frequency of the resonance peak as well as its amplitude shifts with temperature. Furthermore, Fig. 7 (c) illustrates a comparison between measured and synthesized FRFs. The correlation between both FRFs is good, meaning that the modal parameters identified from the curve fit of the PolyMAX algorithm are properly determined.

3.3. *Numerical analysis*

The numerical analysis is performed by applying the IES presented in Section 2.2 for each of the measured mean temperatures. The IES was programmed in Matlab R2021b with an interface to the FE-software MSC Nastran 2022. Nastran was used to solve the complex eigenvalue problem by the complex Lanczos method, shown as step (IIc) in Fig. 2. Both structures are discretized by 8-node CHEXA solid elements with six faces. The spatial displacement of this element type is calculated by linear shape functions, using the linear theory of elasticity. Furthermore, the method of reduced shear integration with bubble functions is selected in MSC Nastran to avoid shear locking and volumetric locking effects. Details about the application of CHEXA elements or about the theory of solid elements in general can be found in [50] and [51], respectively. The element resolution of the FE model is shown in Fig. 8. On the one hand, the resolution was chosen based on a mesh convergence study which showed convergence of the eigenfrequency and loss factor of the first bending mode. On the other hand, the high resolution in width direction resulted from the optimization approach in [30].

The layers are assumed to be perfectly bonded, meaning that the adhesive layer is not modelled and instead, elements of adjacent elastomer and aluminum layers share coincident nodes. Aluminum and BIIR are modeled as isotropic materials and the properties given in Section 3.1 are replicated in the modelling. Furthermore, the sensors are taken into account by concentrated masses (CONM2-elements, each 0.5 g). The first bending mode of both samples is shown in Fig. 9.

4. Results

In this section, eigenfrequencies and damping ratios obtained from the numerical and experimental analyses are compared.

4.1. *Comparison of eigenfrequencies*

Fig. 10 illustrates the comparison of the experimental and numerical eigenfrequencies as a function of temperature. The numerical eigenfrequencies of both specimens are underestimated. An explanation can be the missing modeling of the adhesive layer that would additionally increase the bending stiffness and thus, the eigenfrequencies of the numerical model. Deviations between numerical and experimental data range from less than 1 % to more than 7 %. In general, higher deviations occur for Opt253. A reason could be that Opt253 is more complex to manufacture due to its slim shape (2 mm) which caused difficulties during the conglutination of the layers. However, the qualitative

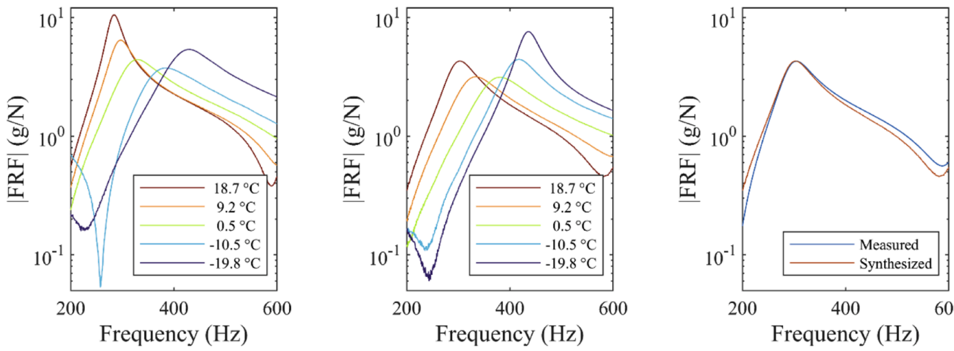

(a) (b) (c)

Fig. 7. Measured FRFs (sensor 1) of specimens (a) Opt253 and (b) Opt293 for different temperatures as well as (c) a comparison between measured and synthesized FRFs of Opt293 at 18.7 °C.

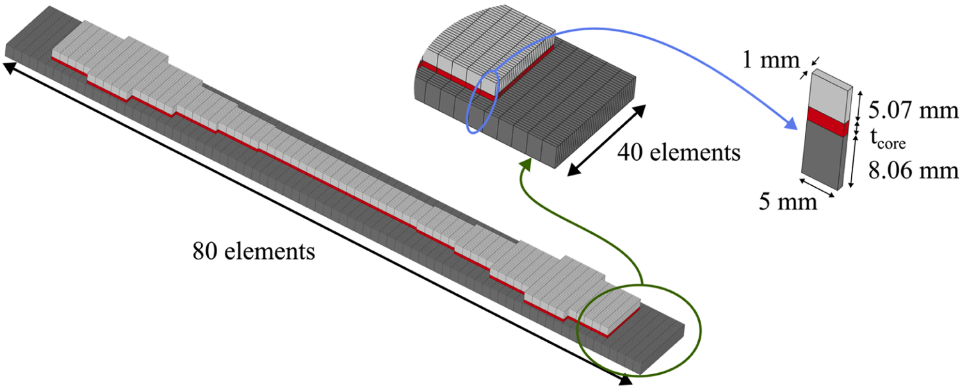

Fig. 8. Element resolution of the FE model exemplified by sample Opt293.

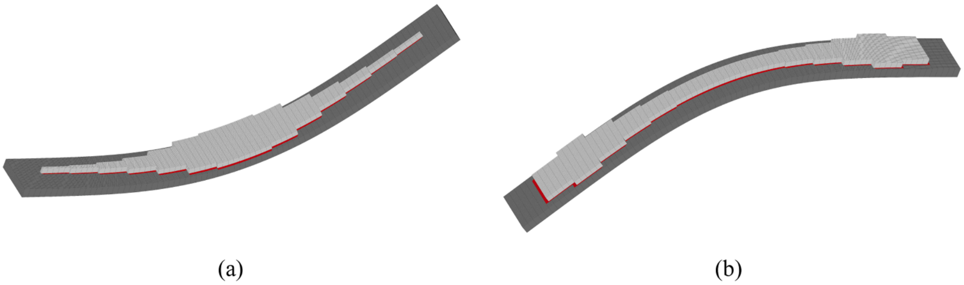

Fig. 9. First bending mode of samples (a) Opt253 and (b) Opt293.

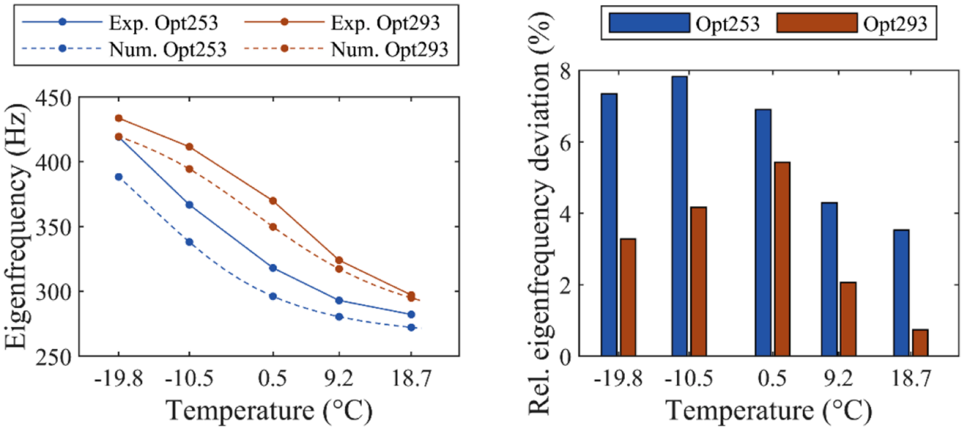

Fig. 10. Numerical and experimental eigenfrequencies (left) and relative eigenfrequency deviation (right) of the first bending mode.

temperature-dependent behavior is validated. The decrease of eigenfrequencies is caused by the softening of BIIR with increasing temperature and is in accordance with the shift of the resonance peak along the frequency axis from Fig. 7 (a).

4.2. *Comparison of damping ratios*

A comparison of the damping ratios is shown in Fig. 11. Apparently, the temperature-dependent trend of the damping ratios could be numerically predicted and fits to the change of amplitudes from Fig. 7 (b). This result validates the design optimization performed in [30] and demonstrates that variable widths of CLD layers are appropriate design parameters for damping optimization. Depending on the shape, the damping performance of the CLD treatments is superior at high or low temperature. While the shape of Opt253 provides high damping at low temperatures and low damping at high temperatures, the opposite applies to Opt293. However, deviations between experimental and numerical damping ratios are clearly visible. In relative values, the deviations range from 4.4 to 23.0 %. The reasons for the deviations are diverse. On the one hand, the synthesized material model does not perfectly match the loss factor data as shown in Fig. 5, leading to smaller numerical damping ratios, in particular at low temperatures. On the other hand, the damping ratios are linked to the eigenfrequencies, since the loss factor of the material is dependent on the eigenfrequency. Therefore, the difference between damping ratios cannot be small, if the deviation between eigenfrequencies is large. Furthermore, the adhesive layer has not been modeled and its influence on the damping performance is not considered.

4.3. *Relation between damping ratio and material loss factor*

An interesting fact observed in Fig. 11 is that the maximum damping

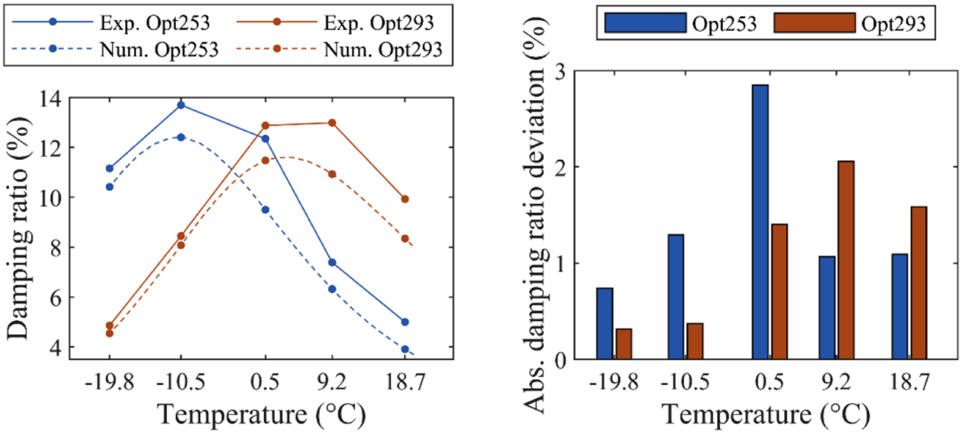

Fig. 11. Numerical and experimental damping ratios (left) and absolute damping ratio deviation (right) of the first bending mode.

ratios are not obtained at the associated design temperatures of both samples. For instance, maximum damping of Opt293 is experimentally identified at 9.2 °C, although it was designed for +20 °C. Even at 0.5 °C the identified damping ratio is higher than for the design temperature. In order to provide an explanation for that, Fig. 12 shows the relation between damping ratios and material loss factors for both samples. The loss factors were calculated by evaluating the Prony series with the measured temperatures and identified eigenfrequencies of each structure.

It can be seen in both diagrams that the maximum loss factor occurs at 0.5 °C. Therefore, the damping ratios of both structures are high at this temperature. However, it is also clear that a high loss factor cannot be the sole cause for high damping. The loss factors at minimum and maximum temperature are approximately equal. Nevertheless, the damping ratios differ significantly. The reason can be traced back to the shear mechanism in the core layer, which is activated either better or worse by the respective design at different temperatures.

4.4. Discussion

The comparison between numerical and experimental modal parameters over a wide temperature range show a good correlation and deviations of eigenfrequencies and damping ratios are comparable to those reported in the literature. The results validate the optimization approach proposed in [30] to use variable widths of the core and face layer as design parameters for damping optimization. It shows that the CLD design can be tailored regarding high damping at a certain design temperature.

However, it is important to emphasize that the optimal design is not directly dependent on the temperature, but on the material properties of the elastomer. Since the material properties vary with temperature, the temperature has just an indirect impact on the design. For instance, another elastomeric material with different sensitivity to temperature would yield different optimal CLD shapes. Therefore, general guidelines towards the optimal shape of CLD treatments are misleading, since the optimal design depends on the operational conditions and material properties.

The damping performance is influenced by the optimized shape in two ways. Firstly, the eigenfrequencies are shifted, changing the loss factor of the elastomer and thus the vibration damping. Secondly, the shear mechanism in the core layer, activating the dissipative properties of the elastomer, is also affected. From the analyses it turned out that both effects need to be considered. Ideally, the eigenfrequency is shifted to a higher loss factor and the elastomeric damping is activated more efficient due to the improved shear mechanism. In opposite, high vibration damping cannot be expected if poor material damping properties are activated or if high material damping properties are not activated.

5. Conclusion

This paper addressed the experimental analysis of shaped-optimized CLD treatments under different ambient temperatures. The results of a modal impact test performed in a climatic chamber were compared to results from a numerical analysis. The comparison showed good agreement. Therefore, the following conclusions can be drawn:

I. Segmenting the core and face layer along the longitudinal axis and using the width of each segment as design parameters is a valid approach for damping optimization. The purpose of the

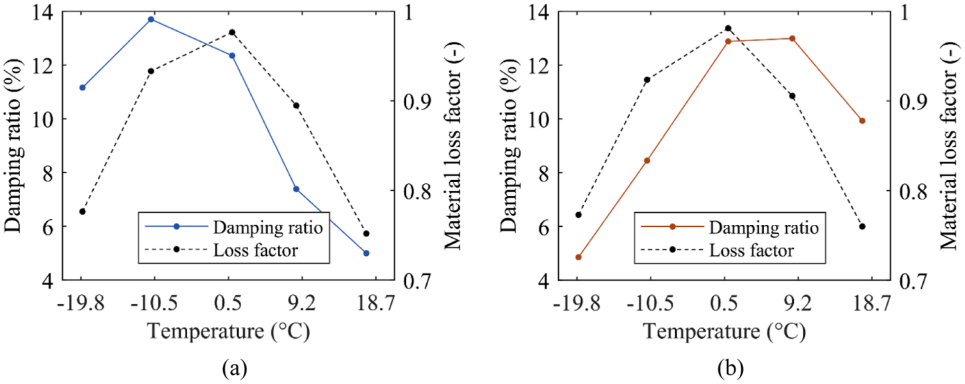

Fig. 12. Relation between damping ratios and material loss factor for (a) Opt253 and (b) Opt293.

shape-optimization is to improve the shear mechanism in the core layer in order to enhance the activation of the elastomeric damping properties.

II. The optimal shape of a CLD treatment depends on the design temperature. However, the temperature has just an indirect impact on the design, since the direct influence comes from the elastomeric material with its temperature-dependent viscoelastic properties.

III. A general guideline for a shape-optimized CLD design cannot be derived. The bandwidth of parameters influencing the design (temperature, material properties, geometry, mode shape, …) is too broad in order to give a well-founded generalized recommendation for the optimal design. Instead, the design should be determined individually by considering all operational conditions.

In future work, the reasons for the deviations of eigenfrequencies and damping ratios will be further analyzed, also considering the modelling and influence of the adhesive layer.

Author agreement statement

We as the authors declare that this manuscript is original, has not been published before and is not currently being considered for publication elsewhere. We confirm that the manuscript has been read and approved by all named authors and that there are no other persons who satisfied the criteria for authorship but are not listed. We further confirm that the order of authors listed in the manuscript has been approved by all of us. We understand that the Corresponding Author is the sole contact for the Editorial process. He/she is responsible for communicating with the other authors about progress, submissions of revisions and final approval of proofs.

CRediT authorship contribution statement

Martin Gröhlich: Writing – original draft, Validation, Software, Methodology, Formal analysis, Conceptualization. **Marc Böswald:** Writing – review & editing, Supervision, Conceptualization. **Jörg Wallaschek:** Writing – review & editing, Supervision, Conceptualization.

Declaration of competing interest

The authors declare that they have no known competing financial interests or personal relationships that could have appeared to influence the work reported in this paper.

Acknowledgements

We would like to acknowledge the funding by the Deutsche Forschungsgemeinschaft (DFG, German Research Foundation) under Germany's Excellence Strategy - EXC 2163/1- Sustainable and Energy Efficient Aviation - Project-ID 390881007.

Furthermore, we would like to thank the Deutsches Institut für Kautschuktechnologie for the vulcanization and characterization of the elastomeric material.

Appendix

Table A
Model parameters of the Prony series of BIIR.

	Index i						
Parameter	1	2	3	4	5	6	7
τ_i (s)	1.000e+04	3.162e+03	1.000e+03	3.162e+02	1.000e+02	3.162e+01	1.000e+01
G_i (Pa)	4.045e+04	4.276e+04	5.985e+04	7.428e+04	5.995e+04	7.379e+04	7.967e+04
	8	9	10	11	12	13	14
τ_i (s)	3.162e+00	1.000e+00	3.162e-01	1.000e-01	3.162e-02	1.000e-02	3.162e-03
G_i (Pa)	8.387e+04	1.049e+05	1.250e+05	1.614e+05	2.278e+05	3.341e+05	5.495e+05
	15	16	17	18	19	20	21
τ_i (s)	1.000e-03	3.162e-04	1.000e-04	3.162e-05	1.000e-05	3.162e-06	1.000e-06
G_i (Pa)	1.002e+06	1.962e+06	3.824e+06	7.580e+06	1.526e+07	2.651e+07	4.224e+07
	22	23	24	25	26	27	∞
τ_i (s)	3.162e-07	1.000e-07	3.162e-08	1.000e-08	3.162e-09	1.000e-09	-
G_i (Pa)	5.911e+07	6.895e+07	9.909e+07	1.610e+08	1.164e+02	2.538e-01	7.473e+05

Table B
WLF and Arrhenius parameters of BIIR.

C_1 (-)	C_2 (K)	T_{ref} (K)	$E_{A,E'}$ (J/mol)	$E_{A,E''}$ (J/mol)
7.26	166.25	293.15	2010	2010

Data availability

Data will be made available on request.

References

[1] M.C.Y. Niu, Airframe Structural Design, 2nd Ed, Conmilit Press, New York, 1988.
[2] Y.-M. Huang, H.-C. Tseng, Active piezoelectric dynamic absorbers on vibration and noise reductions of the fuselage, J. Mech. 24 (Nr. 5) (2008) 69–77.
[3] M. Pisano, E. Turco, G. Petrone, P. Gardonio, S.D. Rosa, Number vs size of electromechanical tuneable vibration absorbers for aeronautical applications: a case study, J. Sound Vib. 561 (2023) 117827.

[4] Y. Zhong, R. Yu, K. Zhou, Z. Zhang, Parameter optimisation of piezoelectric vibration absorber in composite cylindrical shells: A multi-modal approach to mitigate stochastic vibration, Thin-Walled Struct. 207 (2025) 112713.
[5] C. Hesse, Active control of composite fuselage type structures with enclosed acoustic cavity, J. Fluids Struct. 81 (2018) 565–573.
[6] A. Yu, Y. Zhao, Q. Chen, J. liu, Z. Zhou, X. Cao, Vibration transmission analyses of double-layer cylindrical shell with fully immersed elastic connections through experimental and analytical approaches, Thin-Walled Struct. 199 (2024) 111781.
[7] J. Liu, J. Lou, K. Chai, Q. Yang, Nonlinear vibration-acoustic analysis of the coupled system of flexible cylindrical shell foundation and HSLDS vibration isolator, Thin-Walled Struct. 209 (2025) 112896.
[8] X. An, X. Yuan, G. Sun, X. Hou, H. Fan, Design of lattice cylindrical shell metastructures for broadband vibration reduction and high load-bearing capacity, Thin-Walled Struct. 197 (2024) 111647.
[9] Y. Zhang, W. Xu, J. Yang, J. Fu, S. Zhang, Design and study of honeycomb sandwich metastructures for multi-directional low-frequency broadband vibration attenuation, Thin-Walled Struct. 215 (2025) 113459.
[10] L. Rouleau, R. Pirk, B. Pluymers, W. Desmet, Characterization and modeling of the viscoelastic behavior of a self-adhesive rubber using dynamic mechanical analysis tests, J. Aerosp. Technol. Manag. 7 (Nr. 2) (2015) 200–208.
[11] H.F. Brinson, L.C. Brinson, Polymer Engineering Science and Viscoelasticity, Springer, Amsterdam, 2008.
[12] R.L. Bagley, P.J. Torvik, Fractional calculus - A different approach to the analysis of viscoelastically damped structures, AIAA J. 21 (Nr. 5) (1983) 741–748.
[13] D.J. McTavish, P.C. Hughes, Modeling of linear viscoelastic space structures, J. Vib. Acoust. 115 (Nr. 1) (1993) 103–110.
[14] M.L. Williams, R.F. Landel, J.D. Ferry, The temperature dependence of relaxation mechanisms in amorphous polymers and other glass-forming liquids, J. Am. Chem. Soc. 77 (1955) 3701–3707.
[15] A. Nashif, D. Jones, J. Henderson, Vibration Damping, John Wiley & Sons, New York, 1985.
[16] M.D. Rao, Recent applications of viscoelastic damping for noise control in automobiles and commercial airplanes, J. Sound Vib. 262 (Nr. 3) (2003) 457–474.
[17] M.A. Trindade, A. Benjeddou, Hybrid active-passive damping treatments using viscoelastic and piezoelectric materials: review and assessment, J. Vib. Control 8 (Nr. 6) (2002) 699–745.
[18] E.M. Kerwin, Damping of flexural waves by a constrained viscoelastic layer, J. Acoust. Soc. Am. 31 (Nr. 7) (1959) 952–962.
[19] R. DiTaranto, Theory of vibratory bending for elastic and viscoelastic layered finite-length beams, ASME J. Appl. Mech. 32 (Nr. 4) (1965) 881–886.
[20] D.J. Mead, S. Markus, The forced vibration of a three-layer, damped sandwich beam with arbitrary boundary conditions, J. Sound Vib. 10 (Nr. 2) (1969) 163–175.
[21] D. Rao, Frequency and loss factors of sandwich beams under various boundary conditions, J. Mech. Eng. Sci. 20 (Nr. 5) (1978) 271–282.
[22] J.F.A. Madeira, A.L. Araújo, C.M.M. Soares, C.A.M. Soares, Multiobjective optimization for vibration reduction in composite plate structures using constrained layer damping, Comput. Struct. 232 (2020) 105810.
[23] D. Zhang, Y. Wu, X. Lu, L. Zheng, Topology optimization of constrained layer damping plates with frequency- and temperature-dependent viscoelastic core via parametric level set method, Mech. Adv. Mater. Struct. 29 (Nr. 1) (2022) 154–170.
[24] R. Zhu, X. Zhang, S. Zhang, Q. Dai, Z. Qin, F. Chu, Modeling and topology optimization of cylindrical shells with partial CLD treatment, Int. J. Mech. Sci. 220 (2022) 107145.
[25] Q. Zhu, Q. Han, J. Liu, Topological optimization design on constrained layer damping treatment for vibration suppression of thin-walled structures via improved BESO method, Aerosp. Sci. Technol. 142 (2023) 108600.
[26] J. Wang, W. Huang, H. Ji, J. Qiu, Topology optimization of constrained layer damping on acoustic black hole structures for vibration reduction, Appl. Math. Model. 140 (2025) 115904.
[27] G. Lepoittevin, G. Kress, Optimization of segmented constrained layer damping with mathematical programming using strain energy analysis and modal data, Mater. Des. 31 (Nr. 1) (2010) 14–24.
[28] A.L. Araújo, P. Martins, C.M.M. Soares, C.A.M. Soares, J. Herskovits, Damping optimization of viscoelastic laminated sandwich composite structures, Struct. Multidiscip. Optim. 39 (2009) 569–579.
[29] K. Xu, Z. Chen, W. Sun, Optimization of position, size and thickness of viscoelastic damping patch for vibration reduction of a cylindrical shell structure, Compos. Struct. 276 (2021) 114573.
[30] M. Gröhlich, M. Böswald, J. Wallaschek, Viscoelastic damping design - A novel approach for shape optimization of constrained layer damping treatments at different ambient temperatures, J. Sound Vib. 555 (2023) 117703.
[31] M. Leibowitz, J.M. Lifshitz, Experimental verification of modal parameters for 3-layered sandwich beams, Int. J. Solids Struct. 26 (Nr. 2) (1990) 175–184.
[32] E.M. Daya, M. Potier-Ferry, A numerical method for nonlinear eigenvalue problems application to vibrations of viscoelastic structures, Comput. Struct. 79 (Nr. 5) (2001) 533–541.
[33] M. Alvelid, Optimal position and shape of applied damping material, J. Sound Vib. 310 (Nr. 4) (2008) 947–965.
[34] S.Y. Kim, C.K. Mechefske, I.Y. Kim, Optimal damping layout in a shell structure using topology optimization, J. Sound Vib. 332 (Nr. 12) (2013) 2873–2883.
[35] L.T. Stutz, C. Magluta, N. Roitman und R.P. Silva, Experimental and numerical analysis of a sandwich beam with viscoelastic layer, in *Proceedings of the 20th International Congress of Mechanical Engineering*, pp. 15-20, Gramado, Brazil, 2009.
[36] M. Hao, M.D. Rao, Vibration and damping analysis of a sandwich beam containing a viscoelastic constraining layer, J. Compos. Mater. 39 (Nr. 18) (2005) 1621–1643.
[37] V. Sessner, W.V. Liebig, K.A. Weidenmann, Modal damping behavior of plane and 3D curved constrained layer damping CFRP-elastomer-metal laminates, Compos. C: Open Access 2 (2020) 100037.
[38] M. Gröhlich, Numerische und experimentelle Untersuchungen zum optimalen Entwurf von Constrained Layer Damping in Luftfahrtstrukturen, PhD thesis, University Hannover, 2025.
[39] C.M.A. Vasques, R.A.S. Moreira, J.D. Rodrigues, Viscoelastic Damping Technologies - part I: modeling and finite element implementation, J. Adv. Res. Mech. Eng. 1 (Nr. 2) (2010) 76–95.
[40] M. Gröhlich, A. Lang, M. Böswald, J. Meier, Viscoelastic damping design - thermal impact on a constrained layer damping treatment, Mater. Des. 207 (2021) 109885.
[41] A.R. Payne, The dynamic properties of carbon black-loaded natural rubber vulcanizates. Part I, J. Appl. Polym. Sci. 6 (Nr. 19) (1962) 57–63.
[42] A.R. Payne, The dynamic properties of carbon black loaded natural rubber vulcanizates. Part II, J. Appl. Polym. Sci. 6 (Nr. 21) (1962) 368–372.
[43] J. Fritzsche, M. Klüppel, Structural dynamics and interfacial properties of filler-reinforced elastomers, J. Phys.: Condens. Matter 23 (Nr. 3) (2011) 035104.
[44] L. Rouleau, J.-F. Deü, A. Legay, A comparison of model reduction techniques based on modal projection for structures with frequency-dependent damping, Mech. Syst. Signal Process. 90 (2017) 110–125.
[45] Z. Fang, L. Zheng, Topology optimization for minimizing the resonant response of plates with constrained layer damping treatment, Shock Vib. 2015 (2015) 376854.
[46] D.J. Ewins, Modal Testing: theory, practice and application, Research Studies Press Ltd., 2nd Ed., Baldock, Hertfordshire, UK, 2000.
[47] A. Brandt, Noise and Vibration Analysis - Signal Analysis and Experimental Procedures, Wiley, West Sussex, United Kingdom, 2023.
[48] B. Peeters, H.V. der Auweraer, P. Guillaume, J. Leuridan, The PolyMAX frequency-domain method: a new standard for modal parameter estimation? Shock Vib. 11 (2004) 395–409.
[49] P. Guillaume, P. Verboven, S. Vanlanduit, H.V.D. Auweraer und B. Peeters, A poly-reference implementation of the least-squares complex frequency-domain estimator, in *Proceedings of IMAC 21*, Kissimmee, USA, 2003.
[50] M.S.C. Software, MSC Nastran 2022.2 - reference guide, Hexag. AB (2022).
[51] K.J. Bathe, Finite Element Procedures, Prentice Hall, Upper Saddle River, New Jersey, USA, 1996.